

Lateral flow immunoassay using plasmonic scattering

Received: 26 September 2024

Accepted: 25 March 2025

Published online: 09 April 2025

 Check for updates

Bobin Lee  ¹, Byungho Park ¹, Daeun Kim  ^{1,2}, Chaewon Jung ³, Jun Hyeok Park  ³, Ji-Ho Park ³, Young Eun Lee  ⁴, Myung Geun Shin ⁴, Min-Gon Kim ³, Nan Ei Yu ¹, Joon Heon Kim ¹ & Kihyeun Kim  ^{1,5} 

The lateral flow immunoassay (LFIA) is one of the most successful sensing platforms for real-world point-of-care (POC) testing. However, achieving PCR-level sensitivity without compromising the inherent advantages of LFIA, such as rapid and robust operation, affordability, and naked-eye detection, has remained a primary challenge. In this study, a plasmonic scattering-utilising LFIA was proposed, created by transparentising a nitrocellulose membrane and placing a light-absorbing backing card under the membrane. This LFIA minimised the background signal from its matrix, leading to substantially enhanced sensitivity and enabling naked-eye detection of the plasmonic scattering signal from gold nanoparticles without optics. Our plasmonic scattering-utilising LFIA showed an approximately 2600–4400 times higher detection limit compared with that of commercial LFAs in influenza A assays. In addition, it exhibited 90% sensitivity in clinical validation, approaching PCR-level sensitivity, while commercial LFAs showed 23–30% sensitivity. The plasmonic scattering-utilising LFIA plays a ground-breaking role in POC diagnostics and significantly boosts follow-up research.

In principle, point-of-care (POC) testing can play an important role in facilitating timely decision-making in healthcare, leading to improved patient outcomes and enhanced delivery of healthcare services^{1–3}. In practice, although lateral flow immunoassays (LFAs) are particularly valuable for real-world POC testing because of their simplicity, rapid testing, naked-eye detectability, cost-effectiveness, and user-friendliness for non-experts^{4–6}, their relatively low sensitivity is often seen as a critical limitation hindering expansion of its POC application^{7,8}. The limit of detection (LoD) of LFAs is approximately 1000–100,000 times lower than that of PCR tests^{9–11}. Given the increasing attention on personalised and decentralised healthcare—particularly highlighted by the COVID-19 pandemic—enhancing the sensitivity of LFAs to a level comparable to that of PCR has become imperative^{12–14}.

Optical nanoparticles, used as labels in LFAs, are crucial components that determine assay sensitivity. This is because these nanoparticles visualise the sensing signals on the LFIA platforms. Therefore, the effectiveness of visualising these signals through individual optical nanoparticles is critical for achieving high sensitivity. Since their early development, gold nanoparticles (AuNPs) have been extensively utilised in LFAs because of their strong light absorption properties in the visible spectrum¹⁵. The use of AuNPs also enables naked-eye confirmation of testing results, making them highly attractive for POC testing.

Consequently, researchers have focused on developing AuNP-based optical labels to increase the sensitivity of absorption-based LFAs. Two main strategies have been widely adopted: the use of i) large AuNPs¹⁶ and ii) clusters of AuNPs^{17–19} as labels. Although these

¹Advanced Photonics Research Institute (APRI), Gwangju Institute of Science and Technology (GIST), Gwangju 61005, Republic of Korea. ²Department of Biotechnology and Bioengineering, Chonnam National University, Gwangju 61186, Republic of Korea. ³Department of Chemistry, Gwangju Institute of Science and Technology (GIST), Gwangju 61005, Republic of Korea. ⁴Department of Laboratory Medicine, Chonnam National University Medical School and Chonnam National University Hwasun Hospital, Jeollanam-do 58128, Republic of Korea. ⁵ON NANOBIOOLAB Inc., Gwangju 61005, Republic of Korea.

 e-mail: kkh0745@gist.ac.kr

methods have increased sensitivity owing to enhanced light absorption by large AuNPs or AuNP clusters, they have generally achieved only limited improvements in sensitivity. This limitation is often due to the increased size of optical labels over 200 nm in diameter, which reduces their diffusivity and adversely affects the sensitivity of the LFIA^{11,20}. Therefore, alternative approaches are required to improve LFIA performance.

LFIA using fluorescent nanoparticles have been developed to achieve higher sensitivity than traditional AuNP-based LFIA^{21–23}. Fluorescence measurements have an advantage in sensitivity because the use of fluorescence filters and high-intensity light sources enhances the signal-to-noise ratio (SNR) at the test lines. However, the low fluorescence efficiency of typical fluorescent labels has been a major obstacle in improving LFIA sensitivity (the cross-sectional absorption intensity of an 80-nm AuNP was approximately 10⁵ times higher than the fluorescence intensity of a strongly fluorescing dye²⁴). To address this issue, fluorescent dyes have been integrated with plasmonic nanomaterials to enhance their fluorescence efficiency via metal-enhanced fluorescence (MEF), and these labels have been used in LFIA^{25,26}.

Similarly, surface-enhanced Raman scattering (SERS) nanotags have been extensively developed and implemented in LFIA^{27–29}. Although the intensity of the Raman signal from Raman-active materials is generally weak (Raman scattering signals are approximately 10⁷ times weaker than fluorescence signals^{30,31}), SERS nanotags that combine Raman-active molecules and plasmonic nanomaterials emit strong SERS signals due to the formation of plasmonic hotspots within the tags. Consequently, various MEF-based nanoparticles and SERS nanotags have been used to enhance the performance of LFIA.

Although recent studies have shown an increase in the sensitivity of LFIA using MEF-based nanoparticles and SERS tags, novel LFIA with PCR-level sensitivity are still needed for real-world POC testing. In addition, from a POC perspective, LFIA that rely on MEF-based and SERS tag-based technologies are not ideal because these methods require bulky and expensive equipment for result verification, which limits their practical use in the real world.

In this study, a plasmonic scattering-utilising LFIA was presented, which showed similar sensitivity to PCR and enabled naked-eye detection of testing results. Plasmonic scattering is one of the strong signals stemming from when visible light strikes plasmonic nanoparticles, such as AuNPs. For example, the scattering intensity from an 80-nm AuNP can be up to approximately 10⁵ and 10¹² times stronger than the fluorescence intensity from a typical fluorescence dye³² and Raman intensity from a standard Raman reporter^{30–32}, respectively. Therefore, employing plasmonic scattering for signal readout in LFIA has potential for developing an LFIA with improved performance. To construct a plasmonic scattering observation system on LFIA, two key conditions must be met: i) minimising light reflection from the membrane and backing card to reduce background signals; and ii) using plasmonic nanoparticles that strongly scatter visible light. Notably, this type of LFIA facilitates naked-eye detection without additional optics by effectively eliminating background noise intensity on the platform itself. Therefore, plasmonic scattering-utilising LFIA can pave the way for developing a POC testing platform with PCR-level sensitivity for real-world POC testing.

Results

Concept of LFIA using plasmonic scattering

The membranes used in the LFIA reflect the full spectrum of visible light, which explains why the LFIA are white. In conventional LFIA, the plasmonic scattering (hereafter denoted as 'scattering') signal is barely detectable owing to the strong light reflection from the membranes. The reflected light obscures observation of the scattered signal, making it indistinguishable. Thus, minimising light reflection is necessary to effectively observe the scattering signals from AuNPs in LFIA. Reflection can occur on two different components of a conventional LFIA: i) nitrocellulose (NC) membranes and ii) backing cards (Fig. 1a(i)). Thus, the scattering-utilising LFIA was designed with a transparent membrane and light-absorbing layer located underneath the membrane to minimise the reflection of incident light from the matrix (Fig. 1a(ii)).

Unlike conventional LFIA (Fig. 1b(i)), which display red lines originating from AuNP's light absorption on a white background, our LFIA

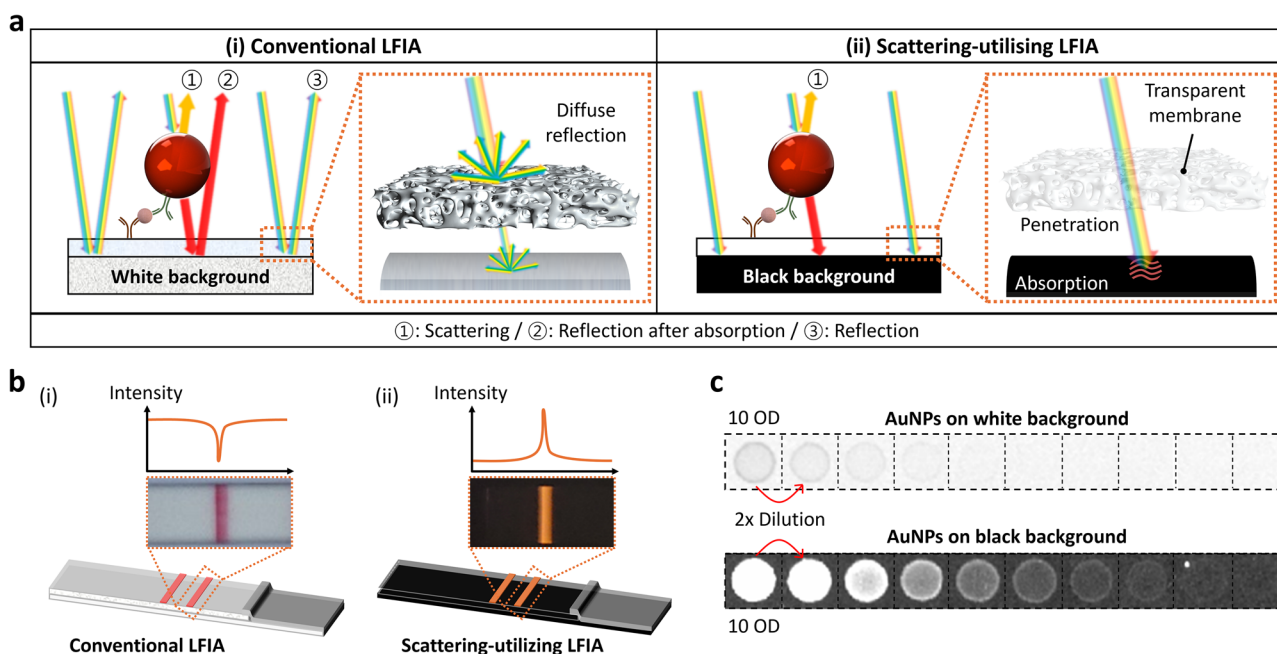


Fig. 1 | Scattering-utilising LFIA concept. **a** Visible light path in the structures of (i) conventional and (ii) scattering-utilising LFIA. **b** Schematic illustration, digital images, and signal intensity profiling of (i) conventional and (ii) scattering-utilising

LFIA. **c** Colourimetric images taken using Chemi-doc equipment with various dilutions of 100 nm AuNP spots on conventional and scattering-utilising LFIA. OD denotes optical density, AuNP gold nanoparticle, LFIA lateral flow immunoassay.

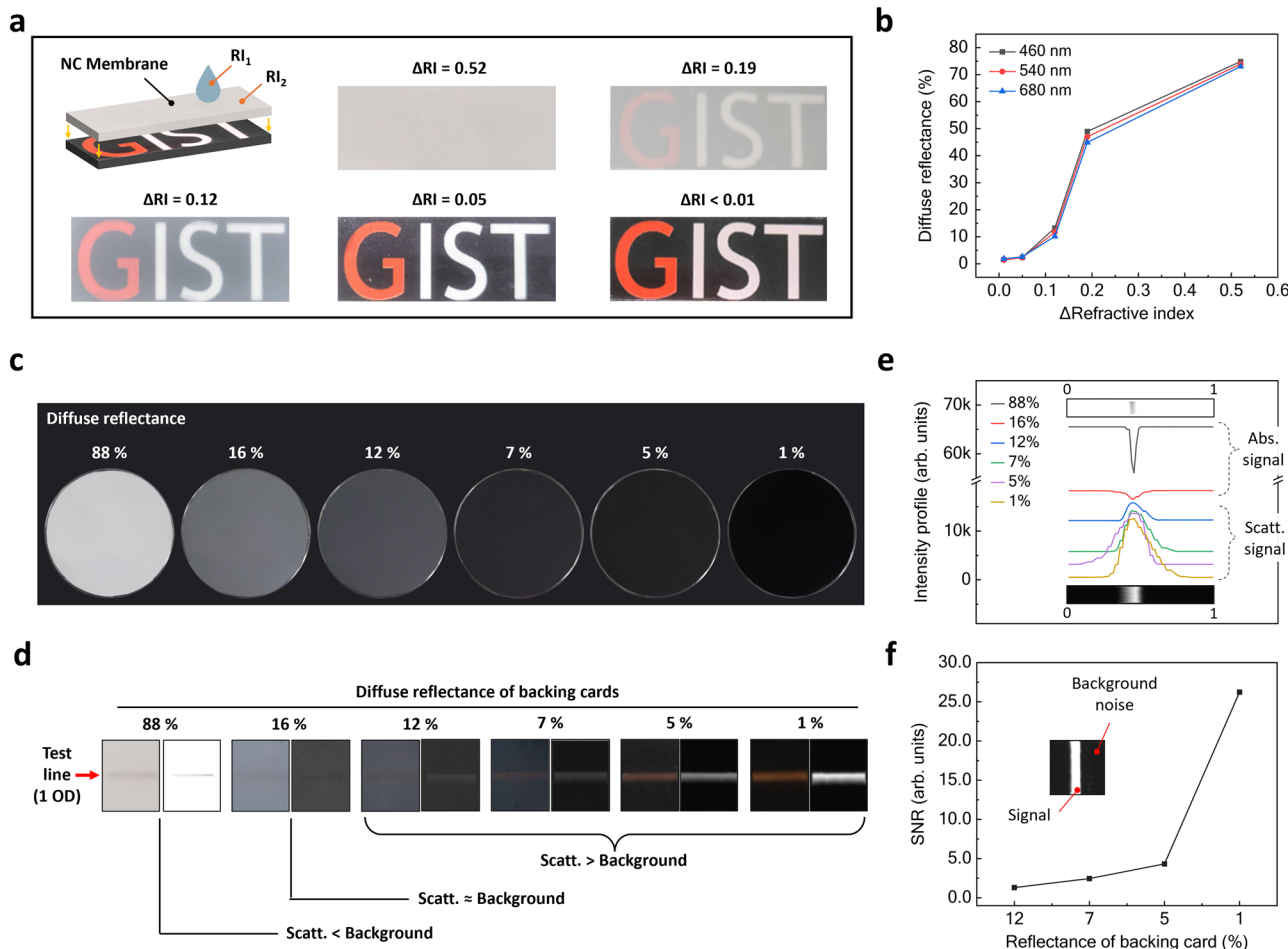


Fig. 2 | Exploring scattering signal detection conditions in LFAs. **a** Photographs showing the transparency of the membrane as a function of RI matching ($\Delta\text{RI} = \text{RI}_2 - \text{RI}_1$) between the filling solution and the NC membrane. **b** Diffuse reflectance of the membrane affected by RI matching. **c** Digital images of backing cards with different diffuse reflectance. **d** Changes in band signal—where the same amount of AuNPs were coated—according to the diffuse reflectance of the backing

cards. Left: images captured using a mobile phone. Right: images measured using Chemi-doc. **e** Profile of the LFIA band signal intensity as a function of background reflectivity. **f** SNR of the LFIA band signal based on the background's reflectivity. LFIA lateral flow immunoassay, NC nitrocellulose, OD optical density, RI refractive index, SNR signal-to-noise.

exhibits orange lines resulting from AuNP's light scattering on a black background (Fig. 1b(ii)). From the perspective of the SNR, our scattering-utilising LFIA (black background LFIA) has higher SNR compared to conventional ones (white background LFIA) because the black background absorbs visible light, leading to an noticeably lower background noise signal. Owing to the higher SNR, the 100-nm AuNPs on the black-background LFIA are more clearly visible than those on a white-background LFIA (Fig. 1c). Thus, scattering-utilising LFAs have the potential to increase sensitivity by reducing noise and increasing the scattering signal from the AuNPs.

Background signal reduction

NC membranes (refractive index, RI, $n = 1.52$) are not transparent when filled with water ($n = 1.33$) or air ($n = 1.0$) because of the diffuse reflection caused by the porous structure of the membrane and the differences in RIs between these media. To minimise diffuse reflection, the RI of the medium filling the pores of the membrane must closely match that of the NC membrane. RI matching was achieved by filling the NC membrane with several media containing different RIs. The membrane became transparent when the RI difference between the medium and NC membrane was nearly zero, as shown in the digital images in Fig. 2a. Diffuse reflection spectroscopy confirmed that the

diffuse reflection of the membrane decreased within the visible spectrum as the ΔRI decreased (Fig. 2b).

Traditionally, the backing cards used in conventional LFAs are white, owing to their lack of visible-light-absorbing properties. Reducing the diffuse reflection from backing cards is important to decrease background noise, leading to a high SNR. To demonstrate this, transparent membranes—where AuNP lines were coated—were placed on backing cards with different reflection intensities (Fig. 2c and Supplementary Fig. 1). Although the same AuNP concentration was captured on all NC membranes, the AuNP-captured lines appeared differently (Fig. 2d). When the diffuse reflectance of the backing card was 88%, the absorption-based signal was observed as a reddish colour and detected using Chemi-doc equipment because the scattering signal intensity from 100 nm AuNPs was weaker than the background noise intensity. When the diffuse reflectance was $<12\%$, the scattering signal predominated because of its stronger intensity compared with that of the background noise signal (Fig. 2e). Consequently, the highest SNR was achieved with the lowest diffuse reflectance (approximately 1%) (Fig. 2f).

Increase in scattering signal of optical labels

To achieve a high SNR, increasing the scattered signal while minimising background noise is essential. According to the Mie theory, the

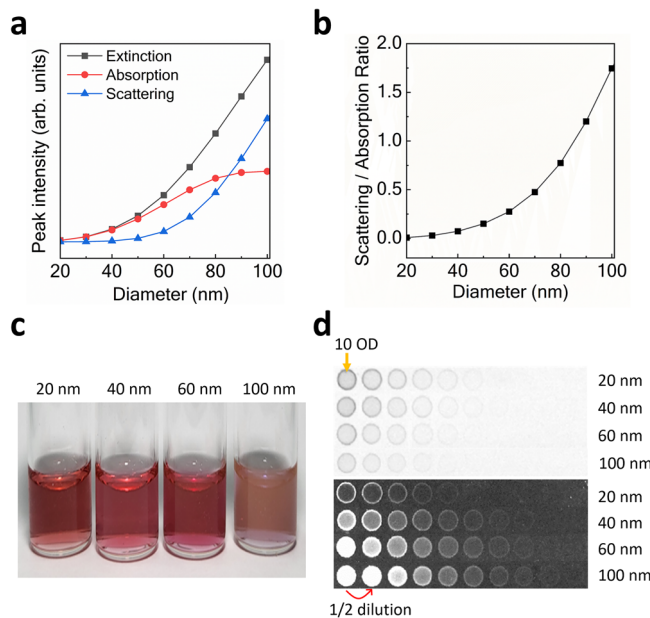


Fig. 3 | Signal variation with AuNP size. **a** Variation in extinction, absorption, and scattering signal peak intensities as a function of gold nanoparticle size. **b** Change in the ratio of scattering signal to absorption signal with increasing gold nanoparticle size. **c** A digital image of AuNP solutions. **d** Colourimetric images, captured by Chemi-doc, of AuNPs spots on a white background (upper) and black background (lower). AuNP gold nanoparticle.

AuNPs on the black background might lead to the decrease in the lowest number of AuNPs being observable). Therefore, the larger AuNPs are the more suitable for plasmonic scattering LFIA.

Influenza A detection using scattering-utilising LFIA

Our scattering-utilising LFIA was operated via a two-step process (Fig. 4a). Initially, the LFIA strip, comprising an NC membrane and visible-light-absorbing backing card, was dipped into a sample solution containing influenza A targets and AuNP-antibody conjugates. Subsequently, a solution for RI matching was applied to the strip. Figure 4b shows the sequentially captured digital images of our scattering LFIA immediately after adding the RI matching solution. When the solution passed through the test line, a transition from absorption to scattering signal occurred. This is because the membrane became transparent owing to RI matching, and the incident visible light was absorbed by the black backing card.

Sensitivity tests of our scattering-utilising LFIAs were conducted using influenza A, and then, compared with those of conventional LFIA (Fig. 4c, d and Supplementary Figs. 2, 3). We used 100-nm AuNPs in our scattering-utilising LFIAs. Although larger AuNPs more strongly scatter light (Fig. 3a), the highest performance was achieved when 100-nm AuNP was used among 20, 40, 60, 150-nm AuNPs (Supplementary Fig. 2a). Notably, in the LFIA, the sensitivity can depend on various factors such as the signal intensities from the AuNPs and background noise, the diffusivity of the AuNPs, and the number of the AuNPs used for LFIA¹¹. Regarding the conventional LFIA, 40-nm AuNPs were used for the conventional LFIA because conventional LFIA generally uses AuNPs with 20–60 nm in diameter where absorption intensity is more important than scattering. In our conventional LFIA, the use of 40–100 nm of AuNPs showed generally good detection performance (Supplementary Fig. 2b). In this research, we used 40-nm AuNPs for conventional LFIAs.

As a result, scattering-utilising LFIAs exhibited significantly higher performance than conventional LFIAs. In viral particle (subtype H1N1) detection assays, the LoD of scattering-utilising LFIAs was 2.09 pfu mL⁻¹, which was a considerable improvement compared to the LoD of 755.47 pfu mL⁻¹ for conventional LFIA (Fig. 4c, d). Similarly, in nucleocapsid protein detection assays, the LoD of scattering signal-utilising LFIAs and conventional LFIA were 1.17 and 234.69 pg mL⁻¹, respectively (Supplementary Fig. 3). Consequently, compared with absorption-based (conventional) LFIAs, our scattering-utilising LFIAs showed 361 times and 201 times enhanced performance when detecting viral particles and nucleocapsid protein, respectively. LoD was defined as mean + 3 × standard deviation of the blank. We compared the LoDs of sensitivity improvement studies for LFIA using various optical nanoparticles (Table 2). We also compared the components' costs of scattering-utilising and conventional LFIAs. Due to the additional components, the carbon black and RI matching solution, there was approximately 11% increase in cost (Supplementary Table 1). Additionally, our LFIA strips demonstrated stability with signal variation within 5% over one year of storage, based on six repeated tests (Supplementary Fig. 4).

To compare our scattering-utilising LFIAs with commercialised testing techniques, three commercial LFIA kits from three companies (denoted as products A, B, and C; Supplementary Fig. 5) were tested for the same viral particle detection. The LoDs were 6375.74, 5417.70, and 9218.84 pfu mL⁻¹ for products A, B, and C, respectively (Fig. 4e). Additionally, qRT-PCR was conducted using the same viral particles, and the results showed that the lowest detectable concentration by qRT-PCR was 1.5 pfu mL⁻¹ (Supplementary Fig. 6). Note that our the LoD of scattering-utilising LFIA was 2.09 pfu mL⁻¹, which was comparable to the qRT-PCR test. Consequently, our scattering-utilising LFIA showed an enhancement in LoD approximately 2600 to 4400 times greater than that of commercial LFIA products.

Selectivity tests were performed using our scattering-utilising LFIA towards the viral particles of SARS-CoV-2, respiratory syncytial

Table 1 | The minimum numbers of AuNPs that could be observable per unit area depending on AuNP sizes

Size of AuNPs	The minimum number of AuNPs that could be detectable per unit area	
	AuNPs on a white background (absorption signal observation)	AuNPs on a black background (scattering signal observation)
20 nm	27,852,116/mm ²	55,704,232/mm ²
40 nm	1,790,493/mm ²	895,247/mm ²
60 nm	1,034,507/mm ²	129,313/mm ²
100 nm	445,634/mm ²	13,926/mm ²

scattering and absorption signals of AuNPs increase along with their size (Fig. 3a). As the particle size increased, the scattering signal grew more rapidly than the absorption signal, causing their ratio to continue increasing until the particle size reached 100 nm (Fig. 3b). A digital image of AuNP solutions was shown in Fig. 3c. Due to strong light scattering of 100-nm AuNPs, the 100-nm AuNP solution was pale orange-coloured. Various AuNP solutions were dropped and dried onto the NC membranes to observe the AuNP signals depending on their diameters (20–100 nm) (Fig. 3d). Although the optical densities of the AuNP solutions were initially the same, smaller AuNPs were more clearly observed on the white background NC membrane. This is consistent with previous studies, which revealed that the absorption properties of AuNPs are more critical than the scattering properties of those in terms of sensitivity in conventional LFIA^{15,17,19}. When the AuNPs were on a black background, larger AuNPs (up to 100 nm) were observed more clearly. Table 1 shows the lowest numbers of AuNPs that could be observable. We obtained the information on the number of the as-purchased AuNP from the manufacturer, BBI Solutions, UK. Based on this information and the optical densities of AuNP solutions, we calculated the number of AuNPs. In particular, for 100 nm AuNPs on a black background, at least 32 times fewer AuNPs could be detected compared with those on a white background (Further dilution of

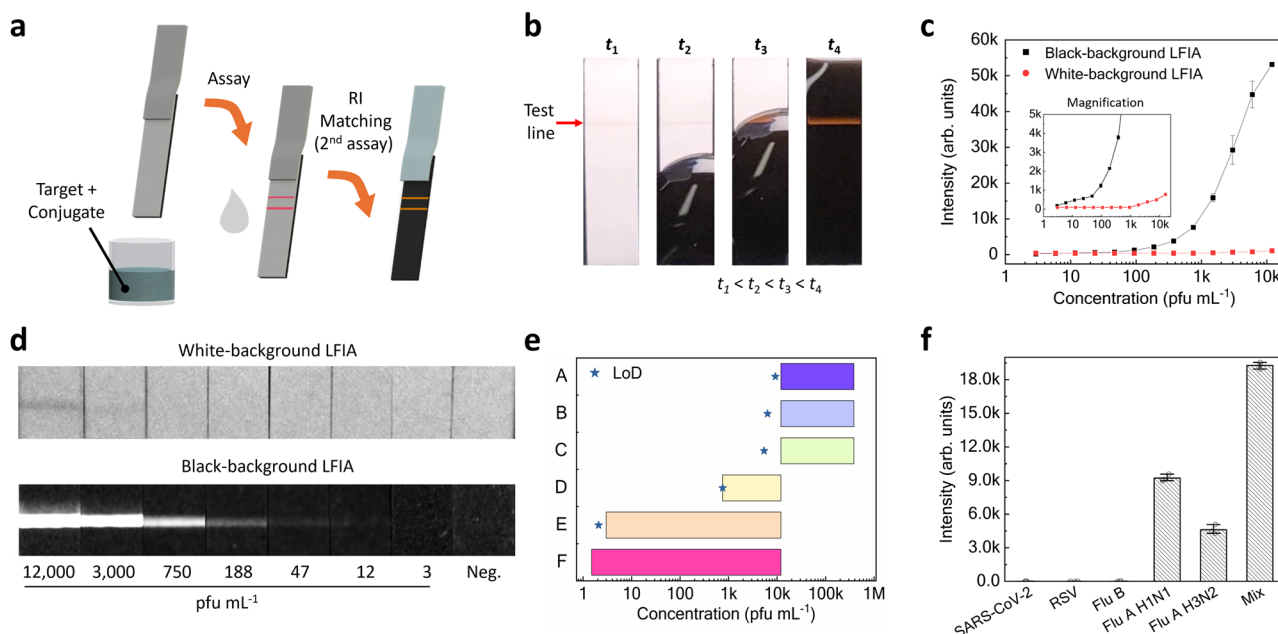


Fig. 4 | Lateral flow assay for influenza A detection. **a** Illustration of assay process for the scattering-utilising LFIA. **b** Photograph showing the signal transition from absorption-based to scattering-utilising. $t_1 = 0$ s, $t_2 = 15$ s, $t_3 = 18$ s, $t_4 = 27$ s. **c** Graph showing the performance of detecting influenza A viral particles with a black-background LFIA (scattering-utilising LFIA) and conventional LFIA. The intensities were calculated as $|$ the average signal value within 10% of the peak intensity $-$ the average background signal value $|$. The spots and error bars indicate average and standard deviation, respectively. Three independent samples were analysed ($n = 3$). **d** Colourimetric images of LFIA after detecting influenza A viral particles.

e Comparison of LoD and detection range of scattering-utilising LFIA, commercial LFIA kits (the products were approved by the Ministry of Food and Drug Safety in

the Republic of Korea), and qRT-PCR. In the graph, the three products were denoted as products A-C; conventional LFIA (fabricated in our group), scattering-utilising LFIA, and qRT-PCR were denoted as D, E, and F, respectively. Boxes indicate the detection range. **f** Selectivity test results for the scattering-utilising LFIA. Concentrations of viral particles: SARS-CoV-2 at 1000 TCID₅₀ mL⁻¹, RSV at 1000 TCID₅₀ mL⁻¹, influenza B at 1000 pfu mL⁻¹, influenza A H1N1 at 1000 pfu mL⁻¹ and H3N2 at 1000 pfu mL⁻¹. Mix contains all samples of the same concentration. The data in the graphs are presented as the mean \pm standard deviation (s.d.); $n = 3$ independent samples. LFIA lateral flow immunoassay, LoD limit of detection, RSV respiratory syncytial virus.

Table 2 | Sensitivity comparison of different influenza A detection methods

Optical label	Probe	Target (influenza A)	Naked eye observation with high sensitivity	Sensitivity of traditional LFIA (control)	Sensitivity
SERS ⁴⁹	AuNP	H1N1	X	– 5×10^4 pfu mL ⁻¹	– 1.9×10^4 pfu mL ⁻¹
SERS ⁵⁰	Au Nanostar	H1N1	X	67 ng mL ⁻¹ –	6.7 ng mL ⁻¹ –
SERS ⁵¹	Fe ₃ O ₄ @Ag	H1N1	X	– 1×10^4 pfu mL ⁻¹	– 50 pfu mL ⁻¹
SERS ⁵²	MGITC + AuNP	H1N1	X	– 1008 HAU mL ⁻¹	– 23 HAU mL ⁻¹
Quantum Dot ⁵³	CdSe/CdS/ZnS QD	H1N1	X	– 160 HAU mL ⁻¹	– 2.5 HAU mL ⁻¹
Quantum Dot ⁵⁴	MnFe ₂ O ₄	H1N1	X	– 5×10^4 pfu mL ⁻¹	– 22 pfu mL ⁻¹
Quantum Dot ⁵⁵	Latex bead@QD	H5N3	X	– 80 HAU mL ⁻¹	– 10 HAU mL ⁻¹
Quantum Dot ⁵⁶	Si@Triple QD	H1N1	X	– 5×10^3 pfu mL ⁻¹	– 50 pfu mL ⁻¹
Fluorescence ⁵⁷	Latex@Red dye 53	H7N1	X	– 160 HAU mL ⁻¹	– 25 ng mL ⁻¹ 80 HAU mL ⁻¹
Fluorescence ⁵⁸	Cy5-doped silica NP	H1N1	X	– 8.8×10 TCID ₅₀ mL ⁻¹	– 250 ng mL ⁻¹ 1.1×10 TCID ₅₀ mL ⁻¹
Fluorescence ⁵⁹	Europium NP	H1N1	X	– 320 HAU mL ⁻¹	– 20 HAU mL ⁻¹
UCNP ⁶⁰	NaYF ₄ :Yb,Tm@NaYF ₄ :Ca	H5N6	X	– $10^{2.5}$ EID ₅₀ mL ⁻¹	– $10^{3.5}$ EID ₅₀ mL ⁻¹
This work	AuNP	H1N1	O	234.69 pg mL ⁻¹ 755.47 pfu mL ⁻¹	1.17 pg mL ⁻¹ 2.09 pfu mL ⁻¹

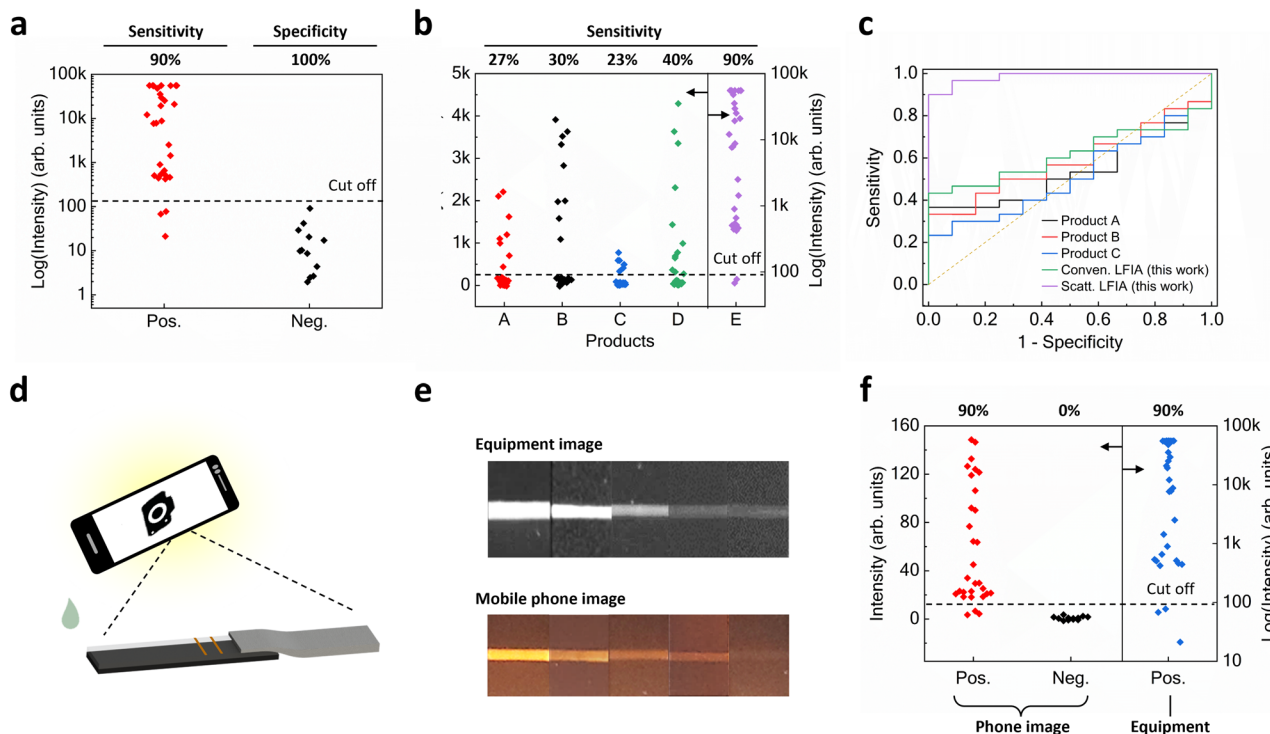


Fig. 5 | Clinical validation. **a** Clinical validation results of the scattering-utilising LFIA. **b** Clinical validation results using three commercial products (A to C), our conventional LFIA (D), and comparison with the scattering-utilising LFIA (E). **c** ROC curve of clinical validation for three commercial products, our conventional LFIA, and the scattering-utilising LFIA. Data for the ROC curve are obtained using Scikit-

learn functions. **d** Method for measuring the scattering signals of an LFIA band using a mobile phone. **e** Image comparison of the scattering-utilising LFIA measured with a Chemi-doc equipment and mobile phone. **f** Clinical validation results of the scattering-utilising LFIA captured with a mobile phone. LFIA lateral flow immunoassay, ROC receiver operating characteristic.

virus (RSV), influenza B, and influenza A (subtypes H1N1 and H3N1). Among the various respiratory viruses, only influenza A virus particles were selectively detected (Fig. 4f).

Our scattering-utilising LFIA were validated using clinical samples collected from patients ($n = 30$) infected with influenza A virus and healthy individuals ($n = 12$). qRT-PCR confirmed that the 30 patients' samples were obtained from infected individuals. The cycle threshold values of the clinical samples are listed in Supplementary Tables 2 and 3. The sensitivity and specificity of our scattering-utilising LFIA were 90% (27 positive results out of 30 infected patient samples) and 100%, respectively (Fig. 5a). Sensitivity and specificity were calculated using Eq. (1) and Eq. (2).

$$\text{Sensitivity} = (\text{true positive}) / (\text{true positive} + \text{false negative}) \quad (1)$$

$$\text{Specificity} = (\text{true negative}) / (\text{true negative} + \text{false positive}) \quad (2)$$

To compare the performance of the scattering-utilising LFIA, conventional LFIA and three LFIA products from three different companies (Supplementary Fig. 7) were tested using the same clinical samples as those used in the scattering-utilising LFIA. The sensitivities of the commercial LFIA ranged from 23% to 30%, significantly lower than that of our scattering-utilising LFIA. Additionally, the conventional LFIA using the same antibody demonstrated a sensitivity of 40% (Fig. 5b). Regarding the receiver operating characteristic (ROC) curves, the products A, B, and C had AUCs of 0.51, 0.59, and 0.54, respectively, and conventional LFIA demonstrated an AUC of 0.62 (Fig. 5c). In contrast, the scattering-utilising LFIA showed improved results, with an AUC of 0.99. Note that the sensitivity of commercial products might appear too low because the clinical samples were swabbed, diluted in a

viral transport medium, and subsequently diluted in a buffer, resulting in very low concentrations. The clinical samples were tested at the same concentration across all platforms. In other words, our scattering-utilising LFIA showed 90% sensitivity despite the use of diluted clinical samples for clinical validation.

One advantage of our scattering-utilising LFIA is that the naked eye can detect the scattering signals without optics. One advantage of our scattering-utilising LFIA is that the naked eye can detect the scattering signals without additional optics. Nonetheless, an extra light source—such as a mobile phone LED—may be required: i) to achieve a strong scattering signal without a dark box, and ii) to avoid interference from ambient light (the intensity of this additional light source should exceed that of the ambient light). Digital images of the clinical validation results were obtained using a mobile phone camera without optics (Fig. 5d, e). Remarkably, the positive detection rate from the images was 90%, the same as that obtained with Chemi-doc equipment (Fig. 5f). Although we used the Galaxy Z-flip 3—launched in 2021—for the comparison, the older Galaxy S8—launched in 2017—also demonstrated similar performance (Supplementary Fig. 8). The mobile phone camera can adjust the exposure time and ISO. Thus, faster image capture is possible when using a mobile phone camera (exposure time: 1/125 s, ISO: 800), compared with that of the Chemi-doc equipment (exposure time: 30 s). Notably, the smartphone performance was similar to that of the Chemi-doc when used with our scattering-utilising LFIAs (Supplementary Fig. 9).

Discussion

Our scattering signal-based LFIA is a type of LFIA beyond those based on absorbance (colourimetric)^{16–19}, fluorescence^{21–23}, SERS^{26–28}, photothermal effect^{33–35}, chemiluminescence^{36–38}, and electrochemiluminescence^{39–42}. To the best of our knowledge, this study reports the concept and realisation of scattering-utilising LFIAs for the first time. Compared with

previous LFAs, scattering-utilising LFAs offer several advantages in terms of sensitivity, stability, reproducibility, naked-eye detection, and ease of integration with mobile phone cameras. The detailed advantages are as follows:

First, plasmonic light scattering from an 80-nm AuNP is 10^5 times higher than light emissions from conventional fluorescent dyes^{24,32} and 10^{11-13} times higher than Raman scattering^{30,31}. Moreover, plasmonic light scattering of an AuNP increases when the diameter of the AuNP increases (Fig. 3a). Therefore, scattering-utilising LFAs using AuNPs with diameters over 80 nm take advantage of enhancing sensing signals among various LFA platforms.

Second, in scattering-utilising LFAs, sensing signals are generated from the inherent properties of AuNPs themselves. The nature of AuNPs is highly stable and biocompatible, which is why AuNPs have been widely used in commercialised LFAs until now^{15,43}. Thus, scattering-utilising LFAs with AuNPs are highly advantageous for achieving high stability and reproducibility. Meanwhile, MEF-based nanoparticles and SERS nanotags, which have recently attracted much attention as optical labels, are difficult to apply in real-world POC testing owing to uncontrollable stability and reproducibility of production^{44,45}.

Third, scattering-utilising LFAs enable naked-eye detection without requiring optical filters or laser-based light sources, making them ideal for POC testing. Meanwhile, research on developing high-performance LFAs is currently based on fluorescence, SERS, photo-thermal effect, chemiluminescence, and electrochemiluminescence. Those approaches require large and expensive equipment for signal readout in general^{23,26-28,33-35,40,41}.

In summary, an AuNP-based scattering-utilising LFA platform was produced by placing a light-absorbing backing card under an NC membrane and matching the RI of the NC membrane with that of a 2nd assay solution. Scattering-utilising LFA platforms were designed to achieve high sensitivity by considering three factors: maximising the transmittance of the NC membrane within the visible wavelength range, minimising background signals, and utilising plasmonic nanoparticles that exhibit high scattering signals. Our scattering-utilising LFAs showed superior performance compared with conventional LFAs. The LoDs of the scattering-utilising LFAs were 2600–4400 times higher than those of commercialised LFAs. In clinical validation, our scattering-utilising LFAs exhibited 90% sensitivity, which was approaching PCR-level sensitivity, whereas that of the commercialised LFAs was within 23–30%.

A potential question may arise regarding the discrepancy between the improved visibility of 100 nm particles on a black background compared to a white background—at least a 32-fold enhancement (Fig. 3d)—and the 361-fold enhancement in the LoD observed in the influenza A assay (Fig. 4c). This discrepancy can be attributed to differences between dry and wet membrane conditions. Figure 3d represents the membrane in a dry state, whereas in the influenza A assay (Fig. 4c), the membrane is saturated with a buffer solution, resulting in a lower Δ RI under assay conditions (RI: air = 1.0, water = 1.33, NC membrane = 1.52). As illustrated in Fig. 2e, a high background reflectance combined with strong light absorption by gold nanoparticles is required in white-background LFA to achieve a high SNR. A wet membrane exhibits a lower SNR compared to a dry membrane, thus reducing sensitivity. Consequently, the scattering-utilising measurement method demonstrates a greater improvement in sensitivity under actual assay conditions than in the dry membrane state.

Scattering-utilising LFAs can be further developed by enhancing the scattering properties of plasmonic nanoparticles used as optical labels. In influenza A assays, 100-nm AuNPs were used because the scattering signal of the 100-nm AuNP is stronger than that of 20–40 nm AuNPs (Fig. 3a). Beyond AuNPs, silver nanoparticles exhibit much stronger scattering intensity compared with the AuNPs (Supplementary Fig. 10). According to the Mie theory, silver nanoparticles exhibit significantly greater scattering cross-section than AuNPs of the

same diameter. Compared to 100-nm AuNP, 100-nm AgNP exhibits a 75% increase in scattering area in the visible range.

A carbon-based dye was used to make black backing cards, which have a diffuse reflectance of approximately 1%. A higher signal-to-noise ratio can be achieved if the reflectivity of the background is further minimised. Reducing the diffuse reflectance of a backing card below 1% can be achieved by incorporating nano- and microstructures onto the black backing card⁴⁶, leading to a further increase in sensitivity^{47,48}.

Thus, those strategies—the enhancement in scattering intensity and the minimisation of the backing card's reflectivity—suggest that with further improvements and optimisations, the sensitivity of scattering-utilising LFAs could be comparable to that of qRT-PCR. In addition, to develop a reliable quantitative analysis, we are currently working on designing suitable housing for both the scattering-utilising LFA and the camera. Scattering-utilising LFAs have great potential for further development as a next-generation LFA platform with PCR-level sensitivity, which can be used by non-expert users worldwide.

Methods

Black-background optimisation

To optimise the background condition via RI matching, a solution composed of 2,2-thiodiethanol (#166782, Sigma-Aldrich) and deionised water was used as the filling medium. The refractive index of filling solution was measured using a refractometer (MyBrix, Mettler Toledo), and the diffuse reflectance of the RI-matched membranes was assessed using UV-Vis spectroscopy (UV-2450 spectrophotometer, Shimadzu). To investigate the characteristics of the black background, a mixture of a carbon-based dye (Musou black, KOYO Orient Japan) and white paint was applied to glass slides to fabricate light-absorbing backgrounds with varying levels of reflectivity. The properties of these backgrounds were analysed using UV-Vis spectroscopy, and their reflectance was compared with BaSO₄ as a reference. Subsequently, membranes made transparent through RI matching were placed on these backgrounds to analyse the scattering properties of the nanoparticles coated on the membranes.

Conjugate preparation

To prepare the conjugate in a borate buffer environment, 100 mL of 0.1 M pH 8.5 borate buffer (#28341; Thermo Fisher Scientific) was mixed with 1 mL of a 1 OD AuNP solution (BBI). Subsequently, 10 μ g of detection antibody (#BRJINFS103, 20220622-1, Fapon) was added, and the mixture was incubated at room temperature (21–23 °C) for 1 h on a rotator. Afterwards, 10 μ L of 10% Casein (#C8654, Sigma-Aldrich) was introduced as a blocking reagent and incubated under the same conditions for an additional hour. The final mixture was centrifuged at 3393 g for 15 min and washed three times with 10 mM borate (pH 8.5) buffer to remove unbound reagents.

Strip preparation

The LFA backing card (TWO HANDS) was initially coated with a carbon-based dye. After the dye had dried, a nitrocellulose membrane (#SHF180UB25, Millipore) was attached. Subsequently, anti-mouse IgG (#M8642, Sigma-Aldrich) at a concentration of 1.0 mg/mL and capture antibodies (#BRCINFS107, 20221130-1, Fapon) at 0.8 mg/mL, both diluted in PBS, were dispensed onto the NC membrane to form the control and test lines, respectively, and allowed to dry (37 °C, 40%) thoroughly. Finally, an absorbent pad (#grade 222, Ahlstrom) was secured, and the completed assembly was cut into individual strips measuring 3.8 mm in width.

Immunoassay

Influenza A H1N1 viral particles (Korea Bank for Pathogenic Viruses) and nucleocapsid protein (#11675, Sino Biological) were detected using the fabricated strips. The assay buffer consisted of 1% Triton

X-100 (#H5142, Promega), 0.4 M NaCl (#S7653, Sigma Aldrich), and 5 mM EDTA (#ER2007-001-80, Biosesang) in 0.1 M Tris-HCl at pH 8.5 (#TR2016-050-85, Biosesang). Test samples were prepared in a buffer containing 10% virus or nucleocapsid protein and a 1 OD conjugate. Next, 50 μ L of test sample was dispensed into each well of a 96-well plate (#32096, SPL), and the dipstick assay was conducted for 15 min. After the assay, the strips were rendered transparent using the RI-matching solution (100% 2,2'-thiodiethanol). Results were captured using a Chemi-doc (#12003153, Bio-Rad Laboratories) and analysed using the Image Lab software (v4.0, Bio-Rad Laboratories). Commercialised products were also tested for sensitivity comparison with our plasmonic scattering-utilising LFIA. Immunoassay using commercialised products was performed using the as-purchased buffers and following the instructions for use (IFU). Results were captured using a Chemi-doc (exposure time 30 s) and a Z-Flip 3 smartphone camera (exposure time: 1/125, ISO: 800; Samsung) and analysed using the Image Lab and Image J software (v1.54 f, NIH), respectively. The intensity of the band signal was obtained by subtracting the average background signal from the average value of the signal within 10% of the peak value (Supplementary Fig. 11). The obtained data were analysed using the Origin program (v10.0.0.154, OriginLab). LoDs were defined as mean + 3 \times standard deviation of the blank.

Clinical validation

Nasopharyngeal and oropharyngeal specimens collected in a viral transport medium were obtained from Chonnam National University Hwasun Hospital (Republic of Korea). All clinical specimens were leftover samples following patient testing. In this case, the Institutional Review Board (IRB) waived the requirement for obtaining informed consent, and the study was approved by IRB of Chonnam National University Hwasun Hospital (CNUHH #: 2023-054). The specimens were anonymized, and since this study focuses on detecting viruses that cause infectious diseases regardless of gender, gender roles were not taken into account in the study design.

In the clinical validation, clinical samples confirmed as positive via qRT-PCR (#CFX96, Bio-Rad Laboratories) were used at a 10% concentration (Supplementary Tables 2 and 3). Regarding the qRT-PCR, the clinical Influenza A samples were extracted using a viral RNA extraction kit and quantified using qRT-qPCR. The primer sequence is the following: The forward primer was 5'-CTT CTA ACC GAG GTC GAA ACG TA-3'. The reverse primer was 5'- GGT GAC AGG ATT GGT CTT GTC TTT A-3'. The probe was 5'- FAM- TCA GGC CCC CTC AAA GCC GAG-BHQ1-3'. The qRT-PCR results were analysed by CFX Connect Real-Time PCR Detection System (Bio-Rad Laboratories).

Regarding the comparison of LFIA, an assay buffer was employed for scattering-utilising LFIA, while commercial products were tested using each manufacturer's specific buffer, following their IFU. The results of tests using clinical samples were measured with Chemi-doc and a smartphone camera (#Z-Flip 3, Samsung) and analysed using the Image Lab and Image J software, respectively.

Reporting summary

Further information on research design is available in the Nature Portfolio Reporting Summary linked to this article.

Data availability

The data presented in this manuscript and generated for this work are included in the written text and figures, as well as provided in the Supplementary Information. Source data are provided with this paper.

References

1. Zhang, G. et al. Molecular Engineering and Confinement Effect Powered Ultrabright Nanoparticles for Improving Sensitivity of Lateral Flow Immunoassay. *ACS Nano* **18**, 2346–2354 (2024).
2. Bahamondes Lorca, V. A. et al. Lateral Flow Assay Biotesting by Utilizing Plasmonic Nanoparticles Made of Inexpensive Metals—Replacing Colloidal Gold. *Nano Lett* **24**, 6069–6077 (2024).
3. Zhang, J. et al. Weakly ionized gold nanoparticles amplify immunoassays for ultrasensitive point-of-care sensors. *Sci. Adv.* **10**, eadn5698 (2024).
4. Wang, T. et al. Development of nucleic acid aptamer-based lateral flow assays: A robust platform for cost-effective point-of-care diagnosis. *Theranostics* **11**, 5174–5196 (2021).
5. Chapman, R. et al. Multivalent Nanoparticle Networks Enable Point-of-Care Detection of Human Phospholipase-A2 in Serum. *ACS Nano* **9**, 2565–2573 (2015).
6. Parolo, C. et al. Tutorial: design and fabrication of nanoparticle-based lateral-flow immunoassays. *Nat. Protoc.* **15**, 3788–3816 (2020).
7. Wang, Z. et al. Four-In-One" Multifunctional Dandelion-Like Gold@platinum Nanoparticles-Driven Multimodal Lateral Flow Immunoassay. *Small* **20**, 2310869 (2024).
8. Choi, D. H. et al. A dual gold nanoparticle conjugate-based lateral flow assay (LFA) method for the analysis of troponin I. *Biosens. Bioelectron.* **25**, 1999–2002 (2010).
9. Gupta, R. et al. Ultrasensitive lateral-flow assays via plasmonically active antibody-conjugated fluorescent nanoparticles. *Nat. Biomed. Eng.* **7**, 1556–1570 (2023).
10. Liu, Y., Zhan, L., Qin, Z., Sackrison, J. & Bischof, J. C. Ultrasensitive and Highly Specific Lateral Flow Assays for Point-of-Care Diagnosis. *ACS Nano* **15**, 3593–3611 (2021).
11. Zhan, L. et al. The Role of Nanoparticle Design in Determining Analytical Performance of Lateral Flow Immunoassays. *Nano Lett* **17**, 7207–7212 (2017).
12. Qin, Z. et al. Significantly Improved Analytical Sensitivity of Lateral Flow Immunoassays by Using Thermal Contrast. *Angew. Chem. Int. Ed.* **51**, 4358–4361 (2012).
13. Rivas, L., Hu, L., Parolo, C., Idili, A. & Merkoçi, A. Rational Approach to Tailor Au-IrO₂ Nanoflowers as Colorimetric Labels for Lateral Flow Assays. *ACS Appl. Nano Mater* **6**, 4151–4161 (2023).
14. Kim, K. et al. Rapid PCR kit: lateral flow paper strip with Joule heater for SARS-CoV-2 detection. *Mater. Horiz.* **10**, 1697–1704 (2023).
15. Wang, Z. et al. An Overview for the Nanoparticles-Based Quantitative Lateral Flow Assay. *Small Methods* **6**, 2101143 (2022).
16. Cui, X. et al. A remarkable sensitivity enhancement in a gold nanoparticle-based lateral flow immunoassay for the detection of Escherichia coli O157:H7. *RSC Adv* **5**, 45092–45097 (2015).
17. Oh, H.-K. et al. Plasmon color-preserved gold nanoparticle clusters for high sensitivity detection of SARS-CoV-2 based on lateral flow immunoassay. *Biosens. Bioelectron.* **205**, 114094 (2022).
18. Sharma, A., Tok, A. I. Y., Alagappan, P. & Liedberg, B. Gold nanoparticle conjugated magnetic beads for extraction and nucleation based signal amplification in lateral flow assaying. *Sens. Actuators B Chem* **312**, 127959 (2020).
19. Chen, X. et al. Self-assembled colloidal gold superparticles to enhance the sensitivity of lateral flow immunoassays with sandwich format. *Theranostics* **10**, 3737–3748 (2020).
20. Li, Y. et al. Integrated gold superparticles into lateral flow immunoassays for the rapid and sensitive detection of *Escherichia coli* O157:H7 in milk. *J. Dairy Sci.* **103**, 6940–6949 (2020).
21. Wang, W. et al. AI-Enhanced Visual-Spectral Synergy for Fast and Ultrasensitive Biodetection of Breast Cancer-Related miRNAs. *ACS Nano* **18**, 6266–6275 (2024).
22. Zhu, Y. et al. Semiconductor Nanoplatelets Based Host-Guest Assembly Structure with High Color Purity for Hue-Recognizable Lateral Flow Immunoassay. *Adv. Funct. Mater.* **34**, 2316147 (2024).
23. Wang, D. et al. Rapid lateral flow immunoassay for the fluorescence detection of SARS-CoV-2 RNA. *Nat. Biomed. Eng.* **4**, 1150–1158 (2020).

24. Jain, P. K., Lee, K. S., El-Sayed, I. H. & El-Sayed, M. A. Calculated Absorption and Scattering Properties of Gold Nanoparticles of Different Size, Shape, and Composition: Applications in Biological Imaging and Biomedicine. *J. Phys. Chem. B* **110**, 7238–7248 (2006).

25. Augustine, S. et al. Metal-enhanced fluorescence biosensor integrated in capillary flow-driven microfluidic cartridge for highly sensitive immunoassays. *Biosens. Bioelectron.* **248**, 115987 (2024).

26. Kim, S. K. et al. Bio-conjugated nanoarchitectonics with dual-labeled nanoparticles for a colorimetric and fluorescent dual-mode serological lateral flow immunoassay sensor in detection of SARS-CoV-2 in clinical samples. *RSC Adv* **13**, 27225–27232 (2023).

27. Zhang, D. et al. Quantitative and ultrasensitive detection of multiplex cardiac biomarkers in lateral flow assay with core-shell SERS nanotags. *Biosens. Bioelectron.* **106**, 204–211 (2018).

28. Wang, C. et al. Ultrasensitive and multiplex detection of four pathogenic bacteria on a bi-channel lateral flow immunoassay strip with three-dimensional membrane-like SERS nanostickers. *Biosens. Bioelectron.* **214**, 114525 (2022).

29. Zhang, D. et al. Rapid and Ultrasensitive Quantification of Multiplex Respiratory Tract Infection Pathogen via Lateral Flow Microarray based on SERS Nanotags. *Theranostics* **9**, 4849–4859 (2019).

30. Matousek, P., Towrie, M. & Parker, A. W. Fluorescence background suppression in Raman spectroscopy using combined Kerr gated and shifted excitation Raman difference techniques. *J. Raman Spectrosc.* **33**, 238–242 (2002).

31. Mosier-Boss, P. A., Lieberman, S. H. & Newberry, R. Fluorescence Rejection in Raman Spectroscopy by Shifted-Spectra, Edge Detection, and FFT Filtering Techniques. *Appl. Spectrosc.* **49**, 630–638 (1995).

32. Jain, P. K., Huang, X., El-Sayed, I. H. & El-Sayed, M. A. Review of Some Interesting Surface Plasmon Resonance-enhanced Properties of Noble Metal Nanoparticles and Their Applications to Biosystems. *Plasmonics* **2**, 107–118 (2007).

33. Liang, M. et al. A versatile nanzyme integrated colorimetric and photothermal lateral flow immunoassay for highly sensitive and reliable *Aspergillus flavus* detection. *Biosens. Bioelectron.* **213**, 114435 (2022).

34. Song, S. et al. Highly sensitive paper-based immunoassay using photothermal laser speckle imaging. *Biosens. Bioelectron.* **117**, 385–391 (2018).

35. Ye, H., Liu, Y., Zhan, L., Liu, Y. & Qin, Z. Signal amplification and quantification on lateral flow assays by laser excitation of plasmonic nanomaterials. *Theranostics* **10**, 4359–4373 (2020).

36. Deng, J., Yang, M., Wu, J., Zhang, W. & Jiang, X. A Self-Contained Chemiluminescent Lateral Flow Assay for Point-of-Care Testing. *Anal. Chem.* **90**, 9132–9137 (2018).

37. Chai, F., Wang, D., Zhu, L., Zheng, W. & Jiang, X. Dual Gold Nanoparticle/Chemiluminescent Immunoassay for Sensitive Detection of Multiple Analytes. *Anal. Chem.* **94**, 6628–6634 (2022).

38. Jung, H. et al. A Size-Selectively Biomolecule-Immobilized Nanoprobe-Based Chemiluminescent Lateral Flow Immunoassay for Detection of Avian-Origin Viruses. *Anal. Chem.* **93**, 792–800 (2021).

39. Zhan, T., Su, Y., Lai, W., Chen, Z. & Zhang, C. A dry chemistry-based ultrasensitive electrochemiluminescence immunosensor for sample-to-answer detection of Cardiac Troponin I. *Biosens. Bioelectron.* **214**, 114494 (2022).

40. Hong, D., Jo, E.-J., Kim, K., Song, M.-B. & Kim, M.-G. Ru(bpy)3²⁺-Loaded Mesoporous Silica Nanoparticles as Electrochemiluminescent Probes of a Lateral Flow Immunosensor for Highly Sensitive and Quantitative Detection of Troponin I. *Small* **16**, 2004535 (2020).

41. Hong, D., Kim, K., Jo, E.-J. & Kim, M.-G. Electrochemiluminescence Incorporated Lateral Flow Immunosensors Using Ru(bpy)3²⁺-Labeled Gold Nanoparticles for the Full-Range Detection of Physiological C-Reactive Protein Levels. *Anal. Chem.* **93**, 7925–7932 (2021).

42. Climent, E. & Rurack, K. Combining Electrochemiluminescence Detection with Aptamer-Gated Indicator Releasing Mesoporous Nanoparticles Enables ppt Sensitivity for Strip-Based Rapid Tests. *Angew. Chem. Int. Ed.* **60**, 26287–26297 (2021).

43. Ma, T. et al. An amphiphilic-ligand-modified gold nanoflower probe for enhancing the stability of lateral flow immunoassays in dried distillers grains. *RSC Adv* **9**, 36670–36679 (2019).

44. Liu, Y.-Q., Zhu, W., Hu, J.-M. & Shen, A.-G. Recent advances in plasmonic Prussian blue-based SERS nanotags for biological application. *Nanoscale Adv* **3**, 6568–6579 (2021).

45. Samanta, A., Jana, S., Das, R. K. & Chang, Y. T. Biocompatible Surface-Enhanced Raman Scattering Nanotags for In Vivo Cancer Detection. *Nanomed.* **9**, 523–535 (2014).

46. Amemiya, K., Shimizu, Y., Koshikawa, H., Shitomi, H. & Yamaki, T. Supreme-black levels enabled by touchproof microcavity surface texture on anti-backscatter matrix. *Sci. Adv.* **9**, eade4853 (2023).

47. Ding, F. et al. Ultrabroadband strong light absorption based on thin multilayered metamaterials. *Laser Photonics Rev* **8**, 946–953 (2014).

48. Niu, C., Zhu, T. & Lv, Y. Influence of Surface Morphology on Absorptivity of Light-Absorbing Materials. <https://doi.org/10.1155/2019/1476217>.

49. Park, H. J., Yang, S. C. & Choo, J. Early Diagnosis of Influenza Virus A Using Surface-enhanced Raman Scattering-based Lateral Flow Assay. *Bull. Korean Chem. Soc.* **37**, 2019–2024 (2016).

50. Maneeprakorn, W., Bamrungsap, S., Apivat, C. & Wiriyachaiporn, N. Surface-enhanced Raman scattering based lateral flow immunochemical assay for sensitive influenza detection. *RSC Adv* **6**, 112079–112085 (2016).

51. Wang, C. et al. Magnetic SERS Strip for Sensitive and Simultaneous Detection of Respiratory Viruses. *ACS Appl. Mater. Interfaces* **11**, 19495–19505 (2019).

52. Lu, M. et al. Dual-mode SERS-based lateral flow assay strips for simultaneous diagnosis of SARS-CoV-2 and influenza a virus. *Nano Converg* **9**, 39 (2022).

53. Nguyen, A. V. T. et al. Sensitive detection of influenza a virus based on a CdSe/CdS/ZnS quantum dot-linked rapid fluorescent immunochemical assay. *Biosens. Bioelectron.* **155**, 112090 (2020).

54. Bai, Z. et al. Rapid Enrichment and Ultrasensitive Detection of Influenza A Virus in Human Specimen using Magnetic Quantum Dot Nanobeads Based Test Strips. *Sens. Actuators B Chem.* **325**, 128780 (2020).

55. Yeo, S.-J. et al. Development of a smartphone-based rapid dual fluorescent diagnostic system for the simultaneous detection of influenza A and H5 subtype in avian influenza A-infected patients. *Theranostics* **8**, 6132–6148 (2018).

56. Wang, C. et al. Development of an ultrasensitive fluorescent immunochemical assay based on multilayer quantum dot nanobead for simultaneous detection of SARS-CoV-2 antigen and influenza A virus. *Sens. Actuators B Chem.* **345**, 130372 (2021).

57. Yeo, S.-J. et al. Rapid detection of avian influenza A virus by immunochemical test using a novel fluorescent dye. *Biosens. Bioelectron.* **94**, 677–685 (2017).

58. Bamrungsap, S., Apivat, C., Chantima, W., Dharakul, T. & Wiriyachaiporn, N. Rapid and sensitive lateral flow immunoassay for influenza antigen using fluorescently-doped silica nanoparticles. *Microchim. Acta* **181**, 223–230 (2014).

59. Yu, S.-T. et al. Clinical evaluation of rapid fluorescent diagnostic immunochemical test for influenza A virus (H1N1). *Sci. Rep.* **8**, 13468 (2018).

60. Kim, J. et al. Rapid and background-free detection of avian influenza virus in opaque sample using NIR-to-NIR upconversion nanoparticle-based lateral flow immunoassay platform. *Biosens. Bioelectron.* **112**, 209–215 (2018).

Acknowledgements

This study was supported by GIST, APRI (K.K.); Industrial Technology Innovation Program (RS-2024-00508652; K.K.) funded by the Ministry of Trade Industry & Energy (MOTIE, Korea); and the National Research Foundation (NRF) of Korea grant funded by the Ministry of Science and ICT (MSIT) (NRF-2021R1A2B5B03001417, M.-G.K.; 2021R1A2C1007130, N.E.Y.; NRF-2021R1A2C1008787, J.H.K.; 2022K1A4A8AO1080317, M.-G.K.).

Author contributions

B.L., J.H.K., and K.K. conceived and designed the research. B.L., B.P., D.K., C.J., J.H.P., J.-H.P., and K.K. designed the experiments. B.L. conducted the LFIA experiments. B.P. performed numerical calculations. C.J., J.H.P., and J.-H.P. conducted PCR tests. B.L., B.P., D.K., and K.K. participated in data analysis and interpretation. Y.E.L. and M.G.S. collected and validated clinical samples. M.-G.K., N.E.Y. J.H.K., and K.K. secured the funding. B.L. and K.K. wrote the paper. K.K. managed this project. All authors reviewed and commented on the paper.

Competing interests

The authors declare no competing interests.

Additional information

Supplementary information The online version contains supplementary material available at <https://doi.org/10.1038/s41467-025-58663-z>.

Correspondence and requests for materials should be addressed to Kihyeun Kim.

Peer review information *Nature Communications* thanks Chuanlai Xu and the other anonymous reviewer(s) for their contribution to the peer review of this work. A peer review file is available.

Reprints and permissions information is available at <http://www.nature.com/reprints>

Publisher's note Springer Nature remains neutral with regard to jurisdictional claims in published maps and institutional affiliations.

Open Access This article is licensed under a Creative Commons Attribution-NonCommercial-NoDerivatives 4.0 International License, which permits any non-commercial use, sharing, distribution and reproduction in any medium or format, as long as you give appropriate credit to the original author(s) and the source, provide a link to the Creative Commons licence, and indicate if you modified the licensed material. You do not have permission under this licence to share adapted material derived from this article or parts of it. The images or other third party material in this article are included in the article's Creative Commons licence, unless indicated otherwise in a credit line to the material. If material is not included in the article's Creative Commons licence and your intended use is not permitted by statutory regulation or exceeds the permitted use, you will need to obtain permission directly from the copyright holder. To view a copy of this licence, visit <http://creativecommons.org/licenses/by-nc-nd/4.0/>.

© The Author(s) 2025